Supporting Information

Optical Kerr Effect of Liquid Acetonitrile Probed by Femtosecond Time-Resolved X-ray Liquidography

Hosung Ki,[1,2,‡] Seungjoo Choi,[3,‡] Jungmin Kim,[1,2] Eun Hyuk Choi,[1,2] Seonggon Lee,[1,2] Yunbeom Lee,[1,2] Kihwan Yoon,[4] Chi Woo Ahn,[1,2] Doo-Sik Ahn,[1,2] Jae Hyuk Lee,[5] Jaeku Park,[5] Intae Eom,[5] Minseok Kim,[5] Sae Hwan Chun,[5] Joonghan Kim,[4] Hyotcherl Ihee,[1,2*] and Jeongho Kim[3*]

[1]*Department of Chemistry and KI for the BioCentury, Korea Advanced Institute of Science and Technology (KAIST), Daejeon 34141, Republic of Korea*
[2]*Center for Nanomaterials and Chemical Reactions, Institute for Basic Science (IBS), Daejeon 34141, Republic of Korea*
[3]*Department of Chemistry, Inha University, 100 Inha-ro, Michuhol-gu, Incheon 22212, Republic of Korea*
[4]*Department of Chemistry, The Catholic University of Korea, Bucheon 14662, Republic of Korea*
[5]*Pohang Accelerator Laboratory, Pohang 37673, Republic of Korea*

[‡]These authors equally contributed to this work.
*Corresponding author. E-mail: hyotcherl.ihee@kaist.ac.kr, jkim5@inha.ac.kr

Supporting Methods

DFT and TDDFT calculations

   We calculated the dipole moment of two different dye molecules, 4-bromo-4′-(*N*,*N*-diethylamino)-azobenzene and Coumarin 153, in ground state and photoexcited state by using density functional theory (DFT) and time-dependent DFT (TDDFT) calculations. Coumarin 153 is a well-known dye molecule that is known to undergo a large dipole moment change upon photoexcitation.[1] We also calculated the change of dipole moment of Coumarin 153 upon photoexcitation as a control to show how large the change of dipole moment in the dye molecule used in this work. The dipole moments were calculated with three different functionals, CAM-B3LYP, MN15, and ωB97XD. The restricted formalism was used in all DFT and TDDFT calculations. The 6-311++G(d,p) basis sets were used. The effect of solvent (acetonitrile) was considered by using the integral equation formalism (IEF) version of the polarizable continuum model (PCM). All calculations were performed using the Gaussian16 program. The molecular structures of the dye molecules and their dipole moment in the ground state were obtained from the DFT calculations. TDDFT calculations were implemented to calculate the oscillator strength of $S_0 \rightarrow S_1$ and $S_0 \rightarrow S_2$ transitions and to calculate the dipole moment in the excited states. The calculated oscillator strength for 4-bromo-4′-(*N*,*N*-diethylamino)-azobenzene was negligible for $S_0 \rightarrow S_1$ transition and was large for $S_0 \rightarrow S_2$ transition. For Coumarin 153, the oscillator strength was large for $S_0 \rightarrow S_1$ transition. Accordingly, the dipole moment of the dye molecules were calculated at S_2 for 4-bromo-4′-(*N*,*N*-diethylamino)-azobenzene and at S_1 states for Coumarin 153, respectively. The dipole moments at the excited states were calculated on the optimized molecular structures of the ground state. The calculation results are listed in Table S1.

SANOD to remove a systematic artifact or the contribution of solvent heating

Systematic artifacts contained in the experimental difference scattering signal were eliminated by using the SANOD method[2], which was reported recently. An example can be seen in Figure S11. The SANOD method was also used to remove the contribution of thermal solvent heating from the experimental difference scattering curves. For $q\Delta S_{iso}$ shown Figure 1g, the contribution of thermal heating was removed from raw $q\Delta S_{iso}$ shown in Figure S5.

Kinetic analysis

For kinetic analysis of $\Delta S_{aniso}(q, t)$, we applied SVD-aided pseudo principal-component analysis (SAPPA)[3]. In this method, the "stationary time zones", where the amplitude of all the principal right singular vectors (rSVs) remain constant, were determined from the SVD analysis of experimental data. Each stationary time zone is regarded as the time delay where only a single transient species exists. In other words, an experimental scattering curve in each of the stationary time zones directly corresponds to a state-associated difference X-ray scattering curve (SAC). Here, we note that $\Delta S_{aniso}(q, t)$ was normalized at each time delay before the SVD analysis. Unless $\Delta S_{aniso}(q, t)$ is normalized, it is difficult to determine the stationary time zones from the SVD analysis because the amplitude of $\Delta S_{aniso}(q, t)$ rapidly decays with time. The SVD analysis of such data would yield right singular vectors (rSVs) of which the values rapidly decrease with time, regardless of the shape change of the signal with time, making it hard to find the stationary time zones, i.e., the time delays where the values of rSV remain constant, from the result of SVD. By contrast, the normalization of $\Delta S_{aniso}(q, t)$ at each time delay makes the amplitude of the signal remain constant over time. By ignoring the change of the amplitude of $\Delta S(q, t)$ with such normalization, we can emphasize how the shape of the signal changes with time and figure out

how many states of different structures are involved in the reaction, based on the assumption that the shape and the amplitude of the scattering signal reflect the structure and the population, respectively, of a state. To quantitatively determine the stationary time zones, we calculated the sum of the absolute values of the first derivative of the two principal rSVs weighted by singular values with respect to $\log_{10}(t)$ in the early-time range.[3] The local minima of the sum of the derivatives were selected as the stationary time zones. Following the criteria, two stationary time zones were found near time zero (at -0.05 ps, photo-aligned state) and at 0.65 ps (2nd intermediate state) as can be seen in Figure S6, and the scattering curves at these time delays were selected as SACs. In fact, two SACs were identified from $\Delta S_{aniso}(q, t)$. For $\Delta S_{iso}(q, t)$ after removing the contribution of solvent heating from the time-resolved scattering data, SVD analysis of $\Delta S_{iso}(q, t)$ yields only a single significant component even without the normalization of the data. Accordingly, one SAC was determined to be the significant lSV of $\Delta S_{iso}(q, t)$.

After determining the SACs, the time-dependent contribution, or the amplitude, of each SAC in the experimental data were estimated. In the case of anisotropic SACs, their amplitudes were determined by solving the following linear equation (linear combination analysis) that approximates the anisotropic scattering responses at a given time delay t as a linear combination of SACs:

$$\Delta S_{aniso}(q,t) = \sum_{i=1}^{2} a_i(t) \cdot SAC_i^{aniso}(q) + X_{aniso}(q,t) \tag{S1}$$

where $SAC_i^{aniso}(q)$ is the i-th anisotropic SAC, $a_i(t)$ is the amplitude of the i-th SACs at the given time delay t, and $X_{aniso}(q, t)$ is the residuals for the approximation. For each time delay, $a_i(t)$ was optimized to minimize χ^2, which is defined as follows:

$$\chi^2 = \sum_{j} (X_{aniso}(q_j,t) / \sigma_{aniso}(q_j,t))^2 \tag{S2}$$

4

where $\sigma_{\mathrm{aniso}}(q_j, t)$ is the standard deviation of $\Delta S_{\mathrm{aniso}}(q, t)$. The resulting $a_i(t)$'s, which are shown in Figure 2, correspond to the population of i-th state at the time delay. In the case of the isotropic SAC, its amplitude was determined simply from the result of SVD. Specifically, the significant rSV was used as the time profile of the amplitude of the isotropic SAC.

The temporal amplitude profiles of the two anisotropic SACs and an isotropic SAC were fitted by a pair of rise and decay exponentials based on a kinetic model. A total of four different states are involved in this kinetic model: equilibrium, photo-aligned, 1$^{\mathrm{st}}$ intermediate, and 2$^{\mathrm{nd}}$ intermediate states. Starting from the equilibrium state, each state forms upon the decay of a preceding state (for example, the 1$^{\mathrm{st}}$ intermediate state forms upon the decay of the photo-aligned state) and subsequently decays to form a trailing state (e.g., the 1$^{\mathrm{st}}$ intermediate state decays to form the 2$^{\mathrm{nd}}$ intermediate state). The formation and decay kinetics of each state were assumed to be mono-exponential, yielding four different time constants. Those time constants correspond to the formation and decay of the photo-aligned state (t_1 and t_2), the decay of the 1$^{\mathrm{st}}$ intermediate state (t_3), and the decay of the 2$^{\mathrm{nd}}$ intermediate state (t_4), respectively. Based on the kinetic model, the theoretical temporal amplitude profiles were generated as follows. The amplitude of SAC$_1^{\mathrm{aniso}}$ instantaneously rises following a rise exponential of time constant t_1 and decays following a decay exponential of time constant t_2. The amplitude of SAC$_2^{\mathrm{aniso}}$ rises following a rise exponential of time constant t_2 and decays following a decay exponential of time constant t_4. The amplitude of SAC$_1^{\mathrm{iso}}$ following a rise exponential of time constant t_1 and decays following a decay exponential of time constant t_3. The temporal amplitude profiles of the three SACs were convoluted with the IRF, which was described by a Gaussian function. By comparing the resultant theoretical temporal amplitude profiles with the temporal amplitude profiles of the experimental SACs, the time constants, t_2, t_3, and t_4, and the width of the Gaussian IRF were optimized. It was assumed that t_1

is too short to be resolved with the IRF of the experiment and thus t_1 was fixed to be close to zero (< 0.1 fs).

Lineshape analysis

The temporal amplitude profile of each SAC was quantitatively analyzed in the frequency domain by using the Fourier transform (FT) lineshape analysis, which was used to resolve the different types of motions in a previous study using time-resolved OKE spectroscopy[4]. In this work, instead of the time-resolved OKE spectroscopic signal used in the literature, the temporal amplitude profile of each SAC was Fourier transformed. The imaginary part of the FT spectrum, $-\text{Im}[FT\{a_i^{\text{iso/aniso}}(t)\}]$, gives the information on the decay rate of the SAC amplitude. The resultant FT spectrum was fitted by using the following lineshape model function:

$$-\text{Im}[FT\{a_i^{\text{iso/aniso}}(t)\}(\omega)]$$
$$= a_l \cdot [\exp(-(\omega-\sigma_l)^2/(2\omega_l^2)) - \exp(-(\omega+\sigma_l)^2/(2\omega_l^2))] + a_{ii} \cdot \omega \cdot \exp(-\omega/\omega_{ii}) \qquad (S3)$$
$$+ a_d \cdot \omega/((\omega-\omega_d)^2 + (1/\sigma_d)^2)$$

where the three terms represent libration, interaction-induced motion, and orientational diffusion, respectively, and the symbols a_l, a_{ii}, a_d, ω_l, ω_{ii}, ω_d, σ_l and σ_d denote the amplitudes (a), frequencies (ω), and widths (σ) of those terms. For the analysis of the FT spectrum for the isotropic SAC, an additional constant, c, was added as a fitting parameter to compensate for the noisy fluctuations in the spectrum, which originate from the low signal-to-noise ratio of the temporal profile of isotropic SAC. Thus, the lineshape model function for the isotropic SAC is as follows:

$$-\text{Im}[FT\{a_i^{\text{iso/aniso}}(t)\}(\omega)]$$
$$= a_l \cdot [\exp(-(\omega-\sigma_l)^2/(2\omega_l^2)) - \exp(-(\omega+\sigma_l)^2/(2\omega_l^2))] + a_{ii} \cdot \omega \cdot \exp(-\omega/\omega_{ii}) \qquad (S4)$$
$$+ a_d \cdot \omega/((\omega-\omega_d)^2 + (1/\sigma_d)^2) + c$$

For the fitting of each SAC, the FT spectrum of a SAC was sufficiently well described even if only one of the three terms were used.

To show that the obtained time constant values are model-independent, we also tried to fit the frequency domain spectrum of each SAC using different lineshape model functions. We tried three different functions shown below:

$$-\mathrm{Im}[FT\{a_i^{\mathrm{iso/aniso}}(t)\}(\omega)] = a_{BO} \cdot \gamma_{BO} \cdot \omega / [(\omega_{BO}^2 - \omega^2)^2 + \gamma_{BO}^2 \cdot \omega^2] \tag{S5}$$

$$\begin{aligned}&-\mathrm{Im}[FT\{a_i^{\mathrm{iso/aniso}}(t)\}(\omega)] \\ &= a_{AG} \cdot [\exp(-2(\omega-\omega_{AG})^2 / \Delta\omega_{AG}^2) - \exp(-2(\omega+\omega_{AG})^2 / \Delta\omega_{AG}^2)]\end{aligned} \tag{S6}$$

$$-\mathrm{Im}[FT\{a_i^{\mathrm{iso/aniso}}(t)\}(\omega)] = a_{ohmic} \cdot \omega_{ohmic} \cdot \exp(-\omega / \omega_{ohmic}) \tag{S7}$$

which are known as a multimode Brownian oscillator model (Eqn. (S5)), an antisymmetrized Gaussian function (Eqn. (S6)), and an Ohmic function (Eqn. (S7)), respectively.[5-7] Note that an antisymmetrized Gaussian function and an Ohmic function are introduced as the 1st term, $a_l \cdot [\exp(-(\omega-\sigma_l)^2 / (2\omega_l^2)) - \exp(-(\omega+\sigma_l)^2 / (2\omega_l^2))]$, and the 2nd term, $a_{ii} \cdot \omega \cdot \exp(-\omega / \omega_{ii})$, respectively, of the lineshape model function shown in Eqns. (S3) and (S4).

MD simulations

We implemented MD simulations to investigate the molecular configurations represented by the SACs obtained from the kinetic analysis of the OKE-XL data. All the simulations were performed by MOLDY 2.16e software employing Nose-Hoover thermostat[8,9] and the periodic boundary condition. The Lennard-Jones parameters and the atomic charge values for the simulation are adapted from a previous study[10]. As described in the main text, we prepared three plausible molecular configurations: (i) the partially aligned configuration corresponding to the photo-aligned state, (ii) the cage-rearranged configuration corresponding to the 2nd intermediate,

and (iii) the randomly oriented configuration corresponding to the equilibrium state. The first configuration was generated by manually changing the angular orientations of a fraction of molecules that are initially in the randomly oriented configuration to the direction of the laser polarization. The latter two configurations (the cage-rearranged configuration and the randomly oriented configuration) were obtained by using the MD simulations. First, we simulated the equilibrium state, that is, randomly-oriented acetonitrile molecules in the liquid phase, by performing MD simulation for 539 acetonitrile molecules contained in a cubic box of 46.75 nm^3 volume. After equilibration for 10 ps at 300 K, 40 snapshots of atomic coordinates of molecules in the box were sampled from the MD trajectory with 1 ps sampling intervals. The sampled snapshots were used as the randomly oriented configuration of the equilibrium state before light irradiation or after the completed relaxation of the photo-aligned molecules. Then, we prepared the partially aligned configuration for the photo-aligned state where some of the liquid molecules are instantaneously aligned upon interaction with light. To do so, we manually reoriented a fraction of the molecules in the randomly oriented configuration toward a direction parallel with the laser polarization, while maintaining the center of mass of each molecule. To see the effect of the number of aligned molecules, we performed the MD simulations with two different fractions of aligned molecules, ~30 % (150 molecules) and ~5 % (27 molecules) of 539 acetonitrile molecules. The former configuration with a larger fraction of aligned molecules was used to emphasize the perturbation of RDF compared with the randomly oriented configuration, as shown in Figure 3. The result of MD simulation for the latter configuration with a smaller fraction of aligned molecules is shown in Figure S12. In this partially aligned configuration, to describe the moment of instantaneous alignment, we did not consider the rearrangement of surrounding molecules in the cage in response to the photoinduced alignment of molecules. The resultant modified snapshots

were used as the partially aligned configuration for the photo-aligned state. To confirm the validity of the modified snapshots as the configuration for the photo-aligned states, we compared the theoretical two-dimensional scattering pattern calculated from the modified snapshots with the experimental pattern at around time zero, and they are in good agreement with each other, as can be seen in Figure S13). Finally, we performed the MD simulation for the cage-rearranged configuration mimicking the 2nd intermediate state, that is, the state formed with the rearrangement of cage molecules via libration and interaction-induced motions in response to the photoinduced alignment of molecules. To do so, we performed another MD simulation for 539 acetonitrile molecules contained in a cubic box of 46.75 nm^3 volume, starting from the initial configuration containing a fraction (~5 %, 27 molecules) of manually aligned molecules along the direction of laser polarization and 512 other molecules without any preferred orientation. In other words, we assumed that the orientations of aligned molecules in the photo-aligned state are still maintained in this cage-rearranged configuration. To simulate the rearrangement of cage molecules, the position and orientation of the 512 molecules were allowed to freely relax by using MD simulation whereas the position and orientation of the initially aligned 27 molecules were kept fixed during the MD simulation. The fixed molecules were placed far enough apart from each other (> 10 Å) to avoid the direct contact between the fixed molecules. By doing so, we tried to focus on the interaction between an aligned molecule and a number of cage molecules, rather than the interaction between the aligned molecules. After equilibration for 10 ps at 300 K, 60 snapshots of atomic coordinates were sampled from the MD trajectory with 1 ps sampling intervals. The sampled snapshots were used as the cage-rearranged configuration.

Calculation of theoretical two-dimensional scattering patterns

To estimate the structural origin of the measured difference X-ray scattering signal, we calculated two-dimensional (2D) scattering patterns from the snapshots obtained from the MD simulations and the modified MD snapshots. The 2D scattering patterns were calculated from the atomic coordinates of the molecules by using the following equation:

$$I(\mathbf{u}, 2\theta, \varphi, \Omega) = \Omega \cdot r_e^2 \cdot I_0 \cdot | \sum_j f_j \cdot \exp(i\Delta k(\mathbf{u}) \cdot \mathbf{x}_j) |^2 \cdot (1 - \sin^2(2\theta) \cdot \cos^2(\varphi)) \qquad (S8)$$

where $\mathbf{u}$ denotes the position of a detector pixel, r_e is the classical radius of an electron, I_0 is the incident X-ray photon flux, f_j is the atomic form factor of the jth atom in the atomic coordinates, $\Delta k(\mathbf{u})$ is a change of the scattering vector, $\mathbf{x}_j$ is the position vector of the jth atom, 2θ is the scattering angle corresponding to the pixel, φ is the azimuthal angle of the pixel, i.e., the angle between a directional vector on the detector plane from the beam center to the detector pixel and the direction of X-ray polarization. This equation calculates the expectation value of the number of elastically scattered photons on the detector pixel, and the incoherent scattering is ignored in this calculation. The detector is positioned 10 cm downstream from the sample and consists of 500 × 500 arrays of 400 μm-sized pixels. The X-ray is assumed to be horizontally polarized, and the energy of the X-ray photon is 15.0 keV (0.827 Å).

Calculation of theoretical difference scattering curves from MD snapshots

We calculated theoretical 2D scattering patterns for the three molecular configurations, i.e., the partially aligned, cage-rearranged, and randomly oriented configurations, by using the structural snapshots obtained from the MD simulations. The scattering patterns were calculated for every structural snapshots (40 snapshots, 60 snapshots, and 40 snapshots for partially aligned, cage-rearranged, and randomly oriented configurations, respectively) and averaged for each

configuration. The averaged patterns for each configuration were decomposed into the isotropic and anisotropic scattering components using the following equations:

$$S^{\text{aligned}}(q,\theta_q) = S_{\text{iso}}^{\text{aligned}}(q) - P_2(\cos\theta_q) \cdot S_{\text{aniso}}^{\text{aligned}}(q,t)$$

$$S^{\text{rearranged}}(q,\theta_q) = S_{\text{iso}}^{\text{rearranged}}(q) - P_2(\cos\theta_q) \cdot S_{\text{aniso}}^{\text{rearranged}}(q,t) \qquad (S9)$$

$$S^{\text{random}}(q,\theta_q) = S_{\text{iso}}^{\text{random}}(q) - P_2(\cos\theta_q) \cdot S_{\text{aniso}}^{\text{random}}(q,t)$$

where aligned, rearranged, and random in the superscript stands for the partially aligned, cage-rearranged, and randomly oriented configurations, respectively. The isotropic and anisotropic scattering components for the partially aligned configuration were calculated with two different fractions of aligned molecules, ~5 % (27 molecules) and ~30 % (150 molecules) of 539 molecules. From the theoretical isotropic and anisotropic scattering components, the theoretical difference scattering curves were calculated as follows:

$$\Delta S_{\text{iso,MD}}^{\text{aligned}}(q) = 1/N_{\text{aligned}}[S_{\text{iso}}^{\text{aligned}}(q) - S_{\text{iso}}^{\text{random}}(q)]$$

$$\Delta S_{\text{aniso,MD}}^{\text{aligned}}(q) = 1/N_{\text{aligned}}[S_{\text{aniso}}^{\text{aligned}}(q) - S_{\text{aniso}}^{\text{random}}(q)]$$

$$\Delta S_{\text{iso,MD}}^{\text{rearranged}}(q) = 1/N_{\text{rearranged}}[S_{\text{iso}}^{\text{rearranged}}(q) - S_{\text{iso}}^{\text{random}}(q)]$$

$$\Delta S_{\text{aniso,MD}}^{\text{rearranged}}(q) = 1/N_{\text{rearranged}}[S_{\text{aniso}}^{\text{rearranged}}(q) - S_{\text{aniso}}^{\text{random}}(q)] \qquad (S10)$$

$$\Delta S_{\text{iso,MD}}^{\text{random}}(q) = [S_{\text{iso}}^{\text{random}}(q) - S_{\text{iso}}^{\text{random}}(q)] = 0$$

$$\Delta S_{\text{aniso,MD}}^{\text{random}}(q) = [S_{\text{aniso}}^{\text{random}}(q) - S_{\text{aniso}}^{\text{random}}(q)] = 0$$

where N_{aligned} and $N_{\text{rearranged}}$ are the number of aligned molecules in the structural snapshots for the partially aligned and cage-rearranged configurations, respectively. We confirmed that both $\Delta S_{\text{iso,MD}}^{\text{aligned}}$ and $\Delta S_{\text{aniso,MD}}^{\text{aligned}}$ are almost the same for the two different fractions of aligned molecules, ~5 % and ~30 % (not shown). In other words, the shapes of theoretical difference scattering curves are not affected by the fraction of aligned molecules in the partially aligned configuration.

Supporting Discussion

Comparison of fs-TRXL and OKE spectroscopy for probing the OKE response

The OKE-XL signal and the time-resolved OKE spectroscopic signal show different dependencies on the solute concentration of a solution, as summarized in Table S3. The solute concentration dependence of the OKE response was systematically studied with time-resolved OKE spectroscopy[4] whereas such dependence has not been investigated with photon echo and time-resolved fluorescence spectroscopies. The overall intensity of the OKE spectroscopic signal increases with the concentration of a resonant dye, with the interaction-induced term showing particularly strong solute concentration dependence for the acetonitrile solvent.[4] For the OKE-XL signal, the interaction-induced term manifested in the isotropic OKE-XL signal is also larger for the dye solution than for neat acetonitrile, but the contributions of libration or orientational diffusion are identical for the solution and neat acetonitrile within the signal-to-noise ratio of the TRXL measurement. Such a stark contrast between spectroscopy and TRXL can be understood by noting that the former detects the light-induced change of refractive index whereas TRXL directly probes the light-induced rearrangement of liquid molecules in real space, which ultimately causes the refractive index change. The light-induced alignment of molecules can be considered to occur randomly, especially well for the molecules that are oriented in the direction close to the laser polarization at the instant of light interaction, and therefore there would be more photo-aligned solvent molecules than the photo-aligned dye molecules, due to the higher number density of solvent molecules than dye molecules in the solution. Since the amplitude of X-ray scattering signal is proportional to the number of molecules, the presence of dye molecules would not affect the OKE-XL signal significantly. In contrast, the OKE spectroscopic signal may still have high sensitivity to the change in the environment (that is, refractive index change) caused by the

12

presence of the dye molecule if the photo-aligned dye molecules act as hot-spots to amplify the change of refractive index, as in the surface Raman scattering signal, despite the smaller number density of dye molecules than solvent molecules. The interaction-induced motion is a collision-induced translational motion and therefore would be affected by the intermolecular interaction, for example, the mass and the size of colliding molecules, more strongly than the other (orientational) motions. The observation that the contribution of interaction-induced motion to the OKE-XL signal depends more strongly on the solute concentration than those of libration and orientational diffusion indicates that the solute-solvent interaction is indeed much stronger than the solvent-solvent interaction.

We also note the differences of TRXL and time-resolved OKE spectroscopy when distinguishing the different types of motions contributing to the relaxation of OKE. In the time-resolved OKE spectroscopic signal, the three types of motions (libration, interaction-induced motion, and orientational diffusion) are manifested as distinct decay components of characteristic rates. In the previous spectroscopic studies[4,11-14], the FT spectrum of the time-resolved spectroscopic signal was decomposed into the contributions of three types of motions based on the theoretical spectra corresponding to those motions in the low-frequency spectral region. In contrast, in the OKE-XL signal, the three different motions can be clearly distinguished from each other, even without relying on the theory, because the three types of motions are manifested in their own distinctive ways in the OKE-XL signal. The contribution of interaction-induced motion appears only in ΔS_{iso}. While both the contributions of libration and orientational diffusion appear only in ΔS_{aniso}, they can be distinguished from each other by their own characteristic shapes in the q-domain. Thus, TRXL has higher selectivity to the different types of motions than time-resolved

spectroscopy, due to the anisotropy of 2D scattering patterns and an extra dimension of q-domain in the OKE-XL data.

Supporting Table

Table S1. Dipole moments of ground and excited states of two dye molecules obtained from DFT and TDDFT calculations.

	Functional	Dipole moment (Debye)[a]		
		Ground state	Excited state	Difference
4-bromo-4′-(*N*,*N*-diethylamino)-azobenzene	CAM-B3LYP	8.3	17.0[b]	8.7
	MN15	8.4	17.1[b]	8.7
	ωB97XD	8.1	16.6[b]	8.5
Coumarin 153[c]	CAM-B3LYP	10.9	16.5[d]	5.6
	MN15	11.0	17.2[d]	6.2
	ωB97XD	10.8	16.4[d]	5.6

[a] The details of the DFT and TDDFT calculations is described in "DFT and TDDFT calculations" section in the Supporting Methods.

[b] In the case of 4-bromo-4′-(*N*,*N*-diethylamino)-azobenzene, the dipole moment calculated for S_2 state is shown because the oscillator strength calculated for $S_0 \rightarrow S_1$ transition is negligible. The oscillator strength is turned out to be large for $S_0 \rightarrow S_2$ transition, indicating that photoexcitation would populate S_2 state.

[c] Coumarin 153 is a well-known dye molecule that is known to undergo a large dipole moment change upon photoexcitation.[1] We also calculated the change of dipole moment of Coumarin 153 upon photoexcitation as a control to show how large the change of dipole moment in the dye molecule used in this work.

[d] In the case of Coumarin 153, the dipole moment calculated for S_1 state is shown because the calculated oscillator strength is large for $S_0 \rightarrow S_1$ transition.[1]

Table S2. Time scales of the three types of motions associated with OKE response.

	$\tau_{\text{libration}}$ (fs)	$\tau_{\text{interaction-induced}}$ (fs)	$\tau_{\text{orientational diffusion}}$ (ps)
Kinetic fit	60 ± 35^a (52 ± 7^b)	350 ± 210^a (150 ± 170^b)	1.5 ± 0.5^a (1.8 ± 0.6^b)
SAC_1^{aniso}	$90\ (89^b), 97^c, 90^d$	-	-
SAC_2^{aniso}	-	-	$1.33\ (1.54^b), 1.54^c,$ 0.9^e
SAC_1^{iso}	-	$377\ (138), 417^c, 278^d$	-
Loughnane *et al.* (OKE spectroscopy experiment, ref. [15])	74^f	$225^f\ (510^g)$	$1.54^f\ (1.64^g)$
Park *et al.* (OKE spectroscopy experiment, ref. [4])	79^f	222^f	1.43^f
Cho *et al.*, (time-dependent fluorescence Stokes peak shift & OKE spectroscopy, ref. [11])	55^h	104^h	-

[a] The time constants were determined from the kinetic fit of the OKE-XL signal of dye solution. Specifically, the experimental data were fitted by a pair of rise and decay exponentials convoluted with a Gaussian-shaped IRF based on a kinetic model. The details of the fitting model are described in the Supporting Method. The time constants obtained by Fourier transform shown in Figure 2 are slightly larger (by ~30 fs) than the values determined by the kinetic fitting because of the broadening of the time profile due to the IRF of a finite width, which was compensated in the kinetic fitting by considering the Gaussian-shaped IRF.

[b] These values in the parentheses were determined from the kinetic fit or FT lineshape analysis of the OKE-XL signal of neat acetonitrile, respectively. Eqn. (S3) is used for the analysis of anisotropic SACs and Eqn. (S4) is used for the analysis of isotropic SAC.

[c] This time constant was determined from the FT lineshape analysis using a multimode Brownian oscillator model (Eqn. (S5)).

^{d} This time constant was determined from the FT lineshape analysis using an antisymmetrized Gaussian function (Eqn. (S6)).

^{e} This time constant was determined from the FT lineshape analysis using an Ohmic function (Eqn. (S7)).

^{f} This time constant was determined from our own lineshape analysis of the data extracted from refs. 4 and 15 using Eqn. (S3).

^{g} These time constants in the parentheses were extracted from ref. 15 as reported, but they are slightly different from the values determined from our own lineshape analysis of the raw data extracted from the same article.

^{h} Values from ref. 11.

Table S3. Comparison of the concentration dependence of the three motions probed by TRXL and OKE spectroscopy. "Yes" means that there is strong dependence and "No" means that there is no or weak dependence.

Technique	(i) libration	(ii) interaction-induced motion	(iii) orientational diffusion
Time-resolved X-ray liquidography	No	Yes	No
Time-resolved OKE spectroscopy	Yes	Yes	Yes

Supporting References

1.   Eom, I.& Joo, T. Polar solvation dynamics of coumarin 153 by ultrafast time-resolved fluorescence. *J. Chem. Phys.* **131,** 244507 (2009).

2.   Ki, H., Lee, Y., Choi, E. H., Lee, S.& Ihee, H. SVD-aided non-orthogonal decomposition (SANOD) method to exploit prior knowledge of spectral components in the analysis of time-resolved data. *Struct. Dyn.* **6,** 024303 (2019).

3.   Oang, K. Y., Yang, C., Muniyappan, S., Kim, J.& Ihee, H. SVD-aided pseudo principal-component analysis: A new method to speed up and improve determination of the optimum kinetic model from time-resolved data. *Struct. Dyn.* **4,** 044013 (2017).

4.   Park, S.*, et al.* Solvent intermolecular polarizability response in solvation. *J. Chem. Phys.* **118,** 3917-3920 (2003).

5.   Shirota, H. Comparison of low-frequency spectra between aromatic and nonaromatic cation based ionic liquids using femtosecond Raman-induced Kerr effect spectroscopy. *ChemPhysChem* **13,** 1638-1648 (2012).

6.   Kakinuma, S.& Shirota, H. Femtosecond Raman-induced Kerr effect study of temperature-dependent intermolecular dynamics in molten bis(trifluoromethylsulfonyl)amide salts: Effects of cation species. *J. Phys. Chem. B* **122,** 6033-6047 (2018).

7.   Kakinuma, S.& Shirota, H. Femtosecond Raman-induced Kerr effect study of temperature-dependent intermolecular dynamics in pyrrolidinium-based ionic liquids: Effects of anion species. *J. Phys. Chem. B* **123,** 1307-1323 (2019).

8.   Nosé, S. A molecular dynamics method for simulations in the canonical ensemble. *Mol. Phys.* **52,** 255-268 (1984).

9.   Hoover, W. G. Canonical dynamics: Equilibrium phase-space distributions. *Phys. Rev. A* **31,** 1695-1697 (1985).

10.   Bernardi, E.& Stassen, H. Molecular dynamics simulations of acetonitrile/dimethyl sulfoxide liquid mixtures. *J. Chem. Phys.* **120,** 4860-4867 (2004).

11.   Cho, M., Rosenthal, S. J., Scherer, N. F., Ziegler, L. D.& Fleming, G. R. Ultrafast solvent dynamics: Connection between time resolved fluorescence and optical Kerr measurements. *J. Chem. Phys.* **96,** 5033-5038 (1992).

12.   Passino, S. A., Nagasawa, Y.& Fleming, G. R. Three pulse stimulated photon echo experiments as a probe of polar solvation dynamics: Utility of harmonic bath models. *J. Chem. Phys.* **107,** 6094-6108 (1997).

13.   Passino, S. A., Nagasawa, Y., Joo, T.& Fleming, G. R. Three-pulse echo peak shift studies of polar solvation dynamics. *J. Phys. Chem. A* **101,** 725-731 (1997).

14.   Fecko, C. J., Eaves, J. D.& Tokmakoff, A. Isotropic and anisotropic Raman scattering from molecular liquids measured by spatially masked optical Kerr effect spectroscopy. *J. Chem. Phys.* **117,** 1139-1154 (2002).

15.   Loughnane, B. J., Scodinu, A., Farrer, R. A., Fourkas, J. T.& Mohanty, U. Exponential intermolecular dynamics in optical Kerr effect spectroscopy of small-molecule liquids. *J. Chem. Phys.* **111,** 2686-2694 (1999).

Supporting Figures
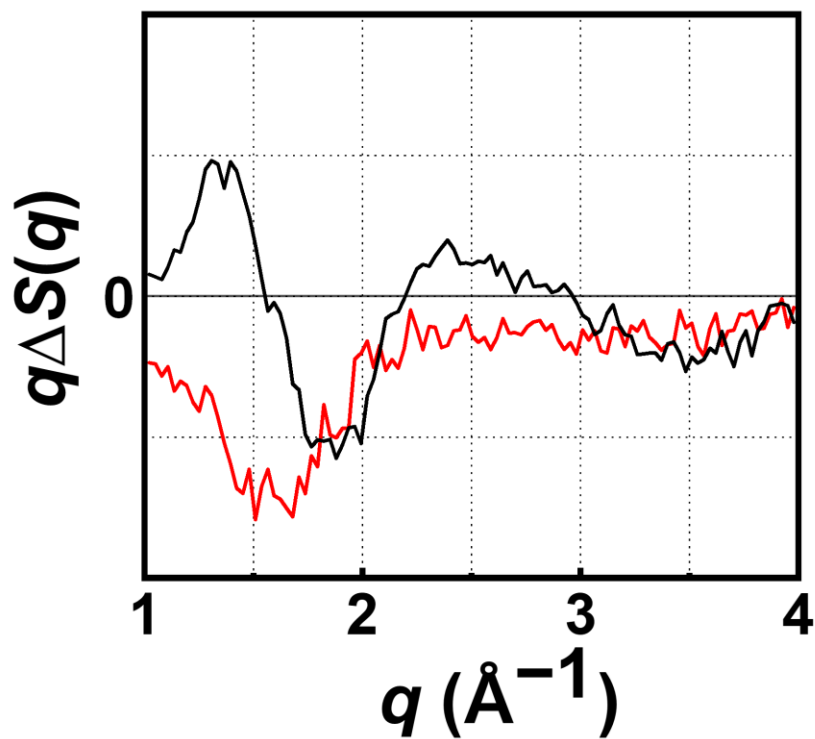
Figure S1. Comparison of difference scattering curves near time zero (t = -0.1 ps, red) and at ~100 ps time delay (black). The difference scattering curves at the two time delays have totally different shapes.
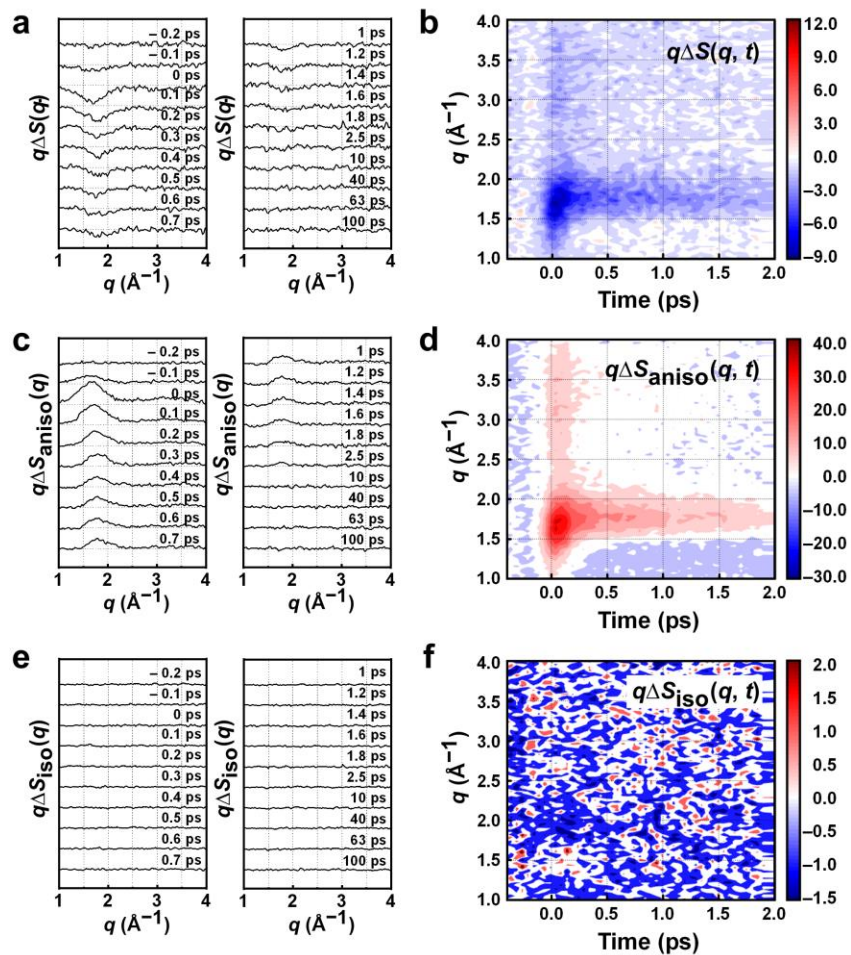
Figure S2. TRXL signals of neat acetonitrile. a–b, Difference scattering curves at individual time delays (**a**) and their contour plot in the early-time range (**b**). **c–d**, Anisotropic scattering response, $q\Delta S_{aniso}$, at individual time delays (**c**) and their contour plot in the early-time range (**d**). **e–f**, Isotropic scattering response, $q\Delta S_{iso}$, at individual time delays (**e**), and their contour plot in the early-time range (**f**).
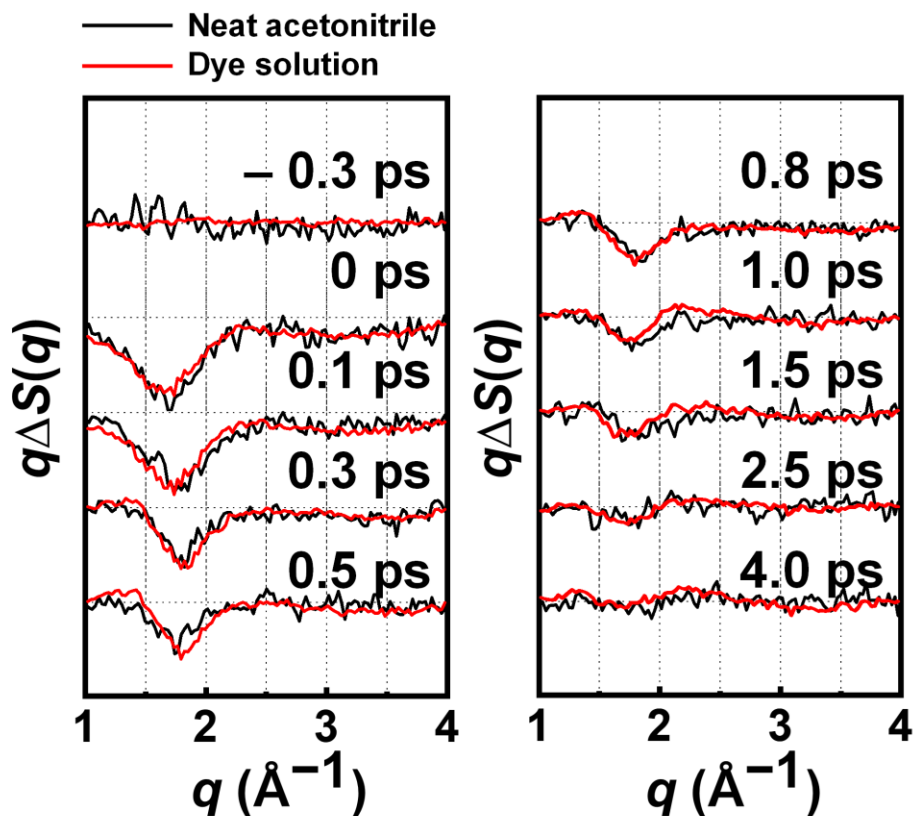
Figure S3. Comparison of time-resolved difference X-ray scattering curves of the dye solution (black) and neat acetonitrile (red) at selected time delays. The contribution of thermal solvent heating to the difference scattering curves for the dye solution was removed by using the SANOD method[2]. The solvent heating contribution is absent for neat acetonitrile due to the absence of light-absorbing molecules resonant with the pump excitation.
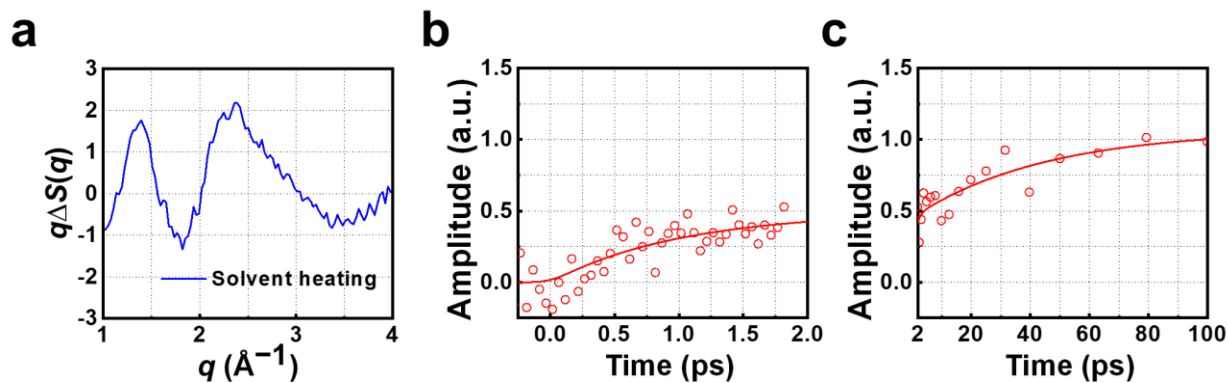
Figure S4. The contribution of solvent heating to ΔS_{iso} of the dye solution. a, The scattering curve arising from the rise of solvent temperature. This scattering curve corresponds to $\Delta S_{iso}(q, t)$ measured at 100 ps time delay. **b–c,** The temporal amplitude profile of the solvent-heating scattering curve manifested in $\Delta S_{iso}(q, t)$ (dots) and its bi-exponential fit (line) in the early-time range (**b**) and late-time range (**c**). From the bi-exponential fitting of the temporal amplitude profile, the time constants for the rise of solvent temperature were determined to be 0.9 ± 1.4 ps and 45 ± 150 ps.
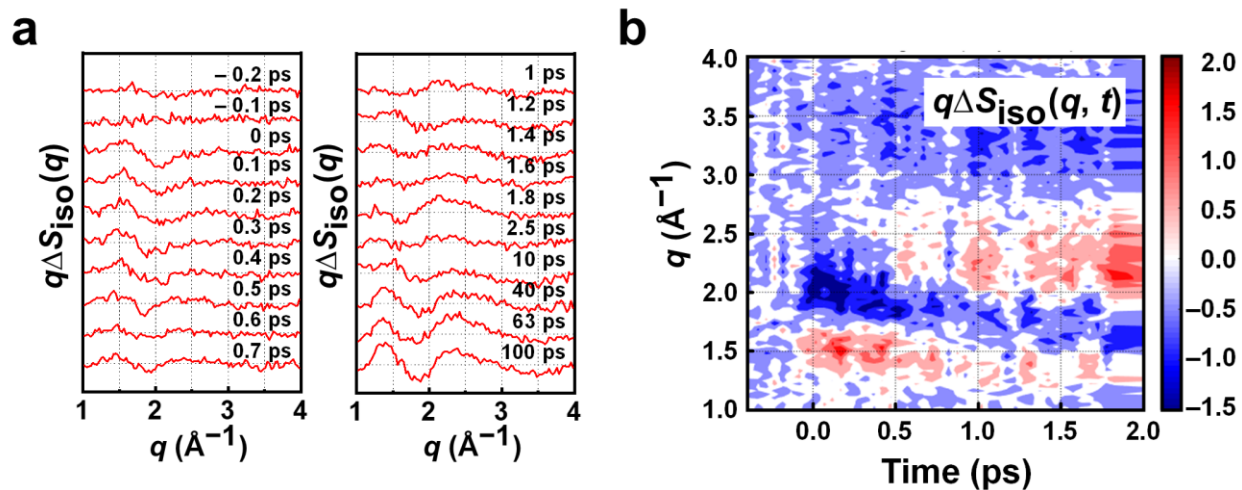
Figure S5. Raw isotropic scattering response, ΔS_{iso}, of the dye solution at individual time delays (a) and their contour plot in the early-time range (b). It can be seen that the scattering curves at the time delays of 40 ps, 63 ps, and 100 ps are significantly different from the ones shown in Fig. 1f because of the presence of solvent heating contribution on the time scale of tens of picoseconds.
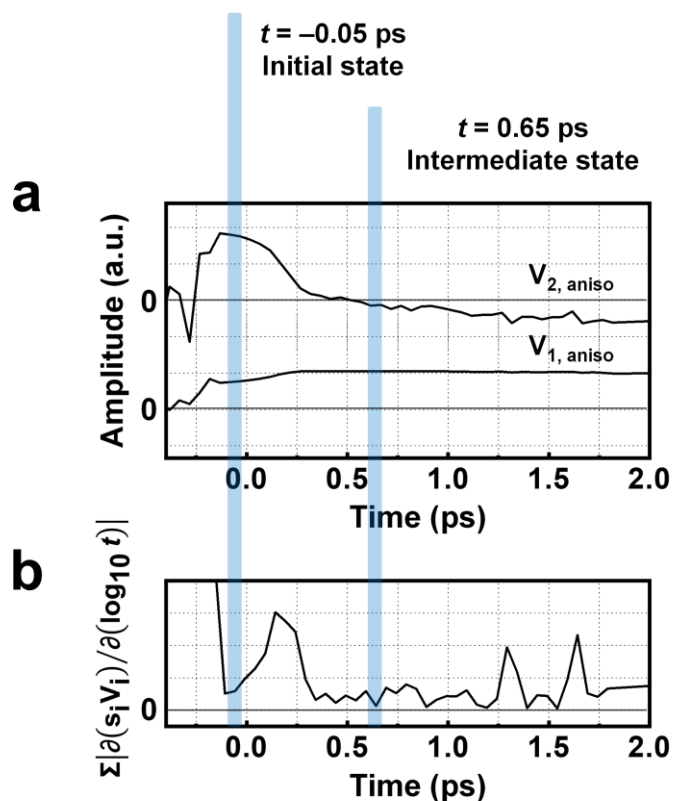
Figure S6. SVD analysis to determine stationary times zones for ΔS_{aniso}. a, Two major rSVs obtained from the SVD analysis of ΔS_{aniso} of the dye solution. Two stationary time zones ($t = -0.05$ ps and 0.65 ps) indicated by blue-shaded areas were determined from the rSVs based on the plots shown in **b** and were utilized for further kinetic analysis based on SAPPA method[3]. **b,** Sums of the absolute values of the first derivatives of the major rSVs weighted by singular values with respect to $\log_{10}t$ for ΔS_{aniso}. Temporal changes of these values were used as the selection criteria of the stationary time zones. Specifically, the time delays corresponding to local minima in these plots for ΔS_{aniso} were selected as the stationary time zones[3] (that is, -0.05 ps and 0.65 ps). In the case of ΔS_{aniso}, the choice of the second stationary time zone (0.65 ps) is rather arbitrary and, in fact, the choice of any time point in the range from 0.3 ps to 2 ps does not affect the analysis significantly. The corresponding plots for ΔS_{iso} (not shown) were ignored due to the low signal-to-noise ratio of ΔS_{iso}. Details of the SVD analysis are described in the SI.
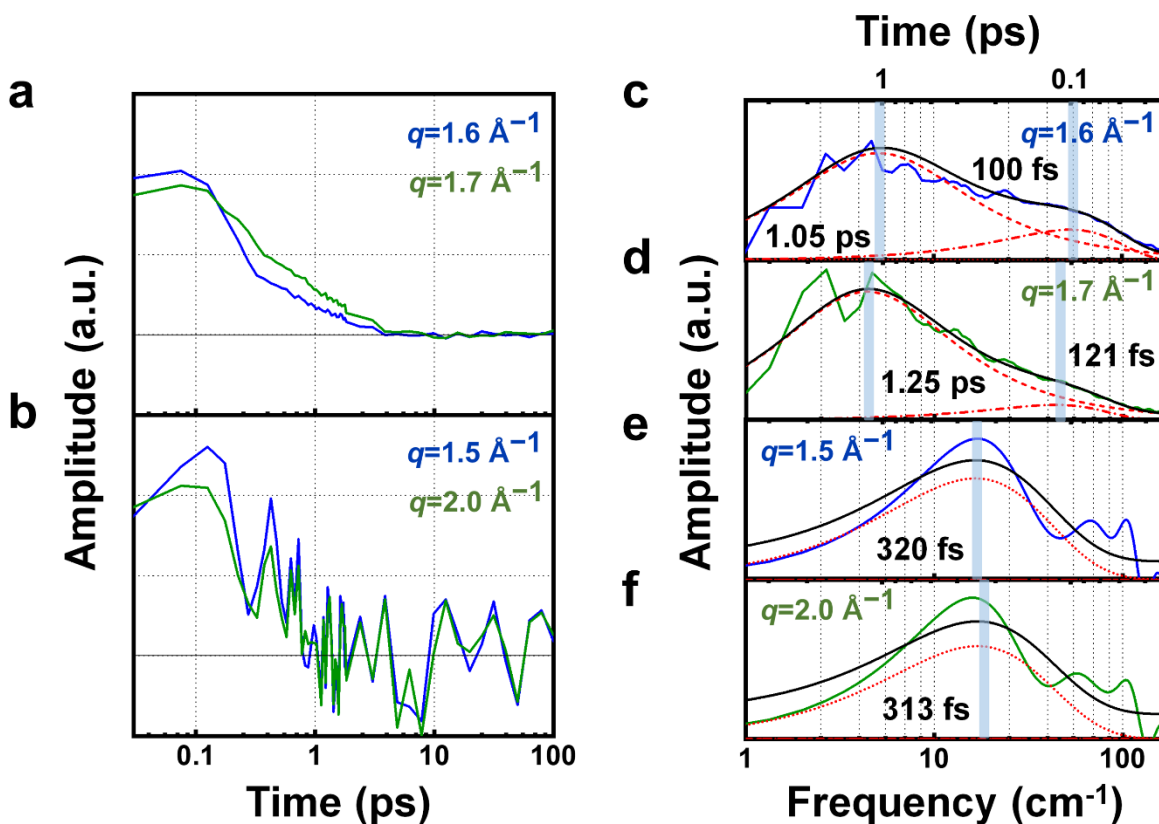
Figure S7. Temporal profiles of ΔS_{iso} and ΔS_{aniso} of the dye solution at selected q points and their FT spectra. a–b, Temporal amplitude profiles of ΔS_{aniso} (**a**) and ΔS_{iso} (**b**) of the dye solution at two selected q points. For ΔS_{aniso}, the selected q points, $q = 1.6$ Å^{-1} (blue) and 1.7 Å^{-1} (green), correspond to the positions of negative peaks of SAC^1_{aniso} and SAC^2_{aniso}, respectively. For ΔS_{iso}, the selected q points, $q = 1.5$ Å^{-1} (blue) and 2.0 Å^{-1} (green), correspond to the positions of positive and negative peaks of SAC^1_{iso}, respectively. **c–f**, FT spectra of the temporal amplitude profiles in **a** and **b**. The imaginary part of an FT spectrum was obtained by Fourier transform of the temporal amplitude profile at the selected q point. The fit (black) of each FT spectrum by a lineshape model function[4] is shown together. The details of the fitting procedure are described in the SI. The peak positions in the FT spectra are indicated by blue vertical bars. The time axis, which was converted from its corresponding frequency axis shown at the bottom, is shown together at the top.
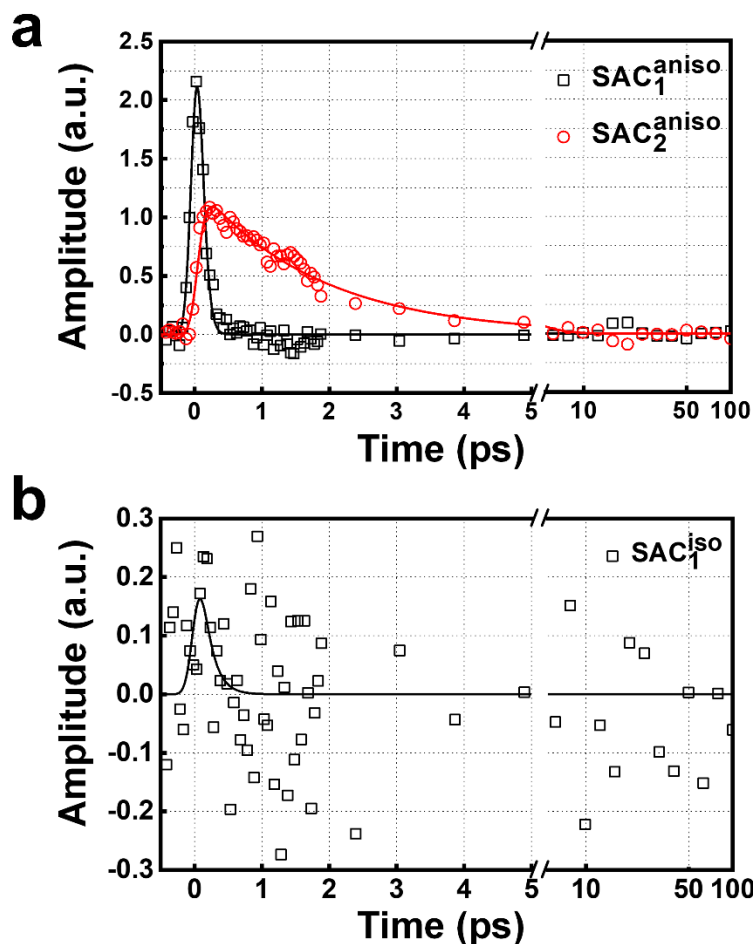
Figure S8. Temporal amplitude profiles of state-associated difference X-ray scattering curves (SACs) of neat acetonitrile. a, Temporal amplitude profiles of the anisotropic SACs, SAC_1^{aniso} (black dots) and SAC_2^{aniso} (red dots) with their theoretical fits (black and red lines, respectively) shown together. The details of the fitting procedure are described in the SI. The time constants of the decay exponentials were determined to be 52 ± 7 fs for SAC_1^{aniso} and 1.8 ± 0.6 ps for SAC_2^{aniso}. **b**, Temporal amplitude profile of the isotropic SAC, SAC_1^{iso} (black dots), with its fit (black line) shown together. The time constant of the decay exponential was determined to be 150 ± 170 fs for SAC_1^{iso}.
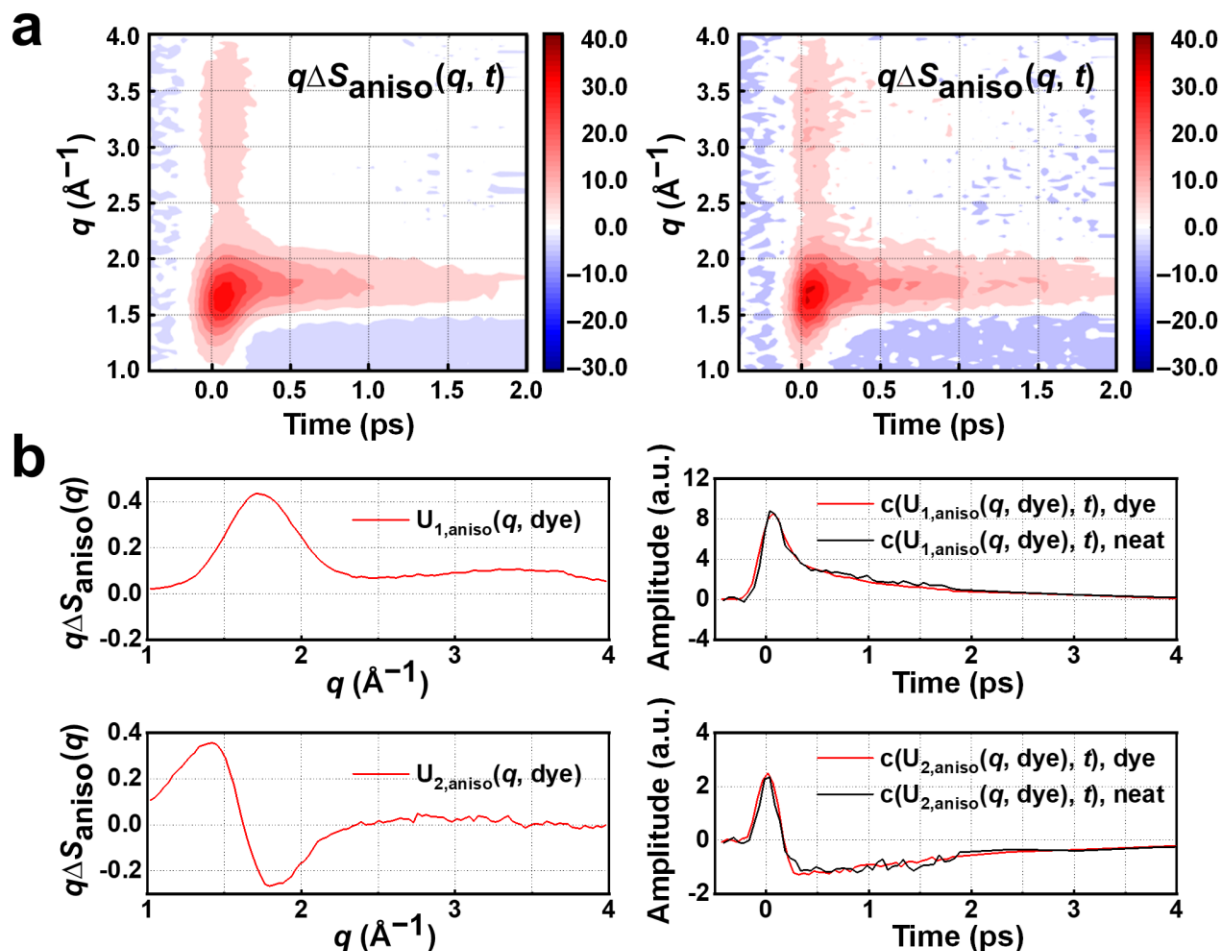
Figure S9. Comparison of $\Delta S_{aniso}(q, t)$'s of the dye solution and neat acetonitrile. a, Contour plots of $\Delta S_{aniso}(q, t)$ of the dye solution (left) and neat acetonitrile (right). **b**, (Left) Two significant lSVs of $\Delta S_{aniso}(q, t)$ of the dye solution, $U_{1,aniso}(q, dye)$ and $U_{2,aniso}(q, dye)$. Here the lSVs were multiplied by q to clearly visualize the fluctuation of the amplitudes at high scattering angles. (Right) Temporal amplitude profiles of the two significant lSVs. The temporal amplitude profiles of the lSVs for the dye solution were obtained by multiplying the corresponding rSV by its singular value. The temporal amplitude profiles of the lSVs for neat acetonitrile were obtained by linear combination analysis of $\Delta S_{aniso}(q, t)$ of neat acetonitrile with the two $U_{aniso}(q, dye)$'s. Note that the lSVs of the dye solution have nearly the same amplitude as those of neat acetonitrile.
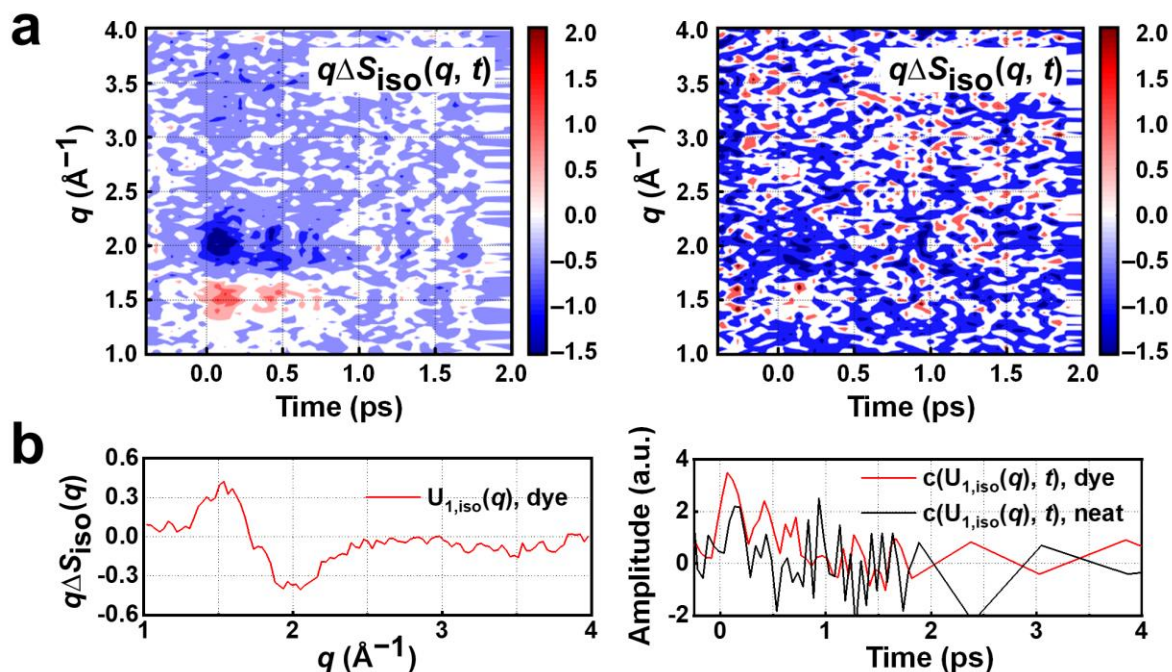
Figure S10. Comparison of $\Delta S_{iso}(q, t)$'s of the dye solution and neat acetonitrile. a, Contour plots of $\Delta S_{iso}(q, t)$ of the dye solution (left) and neat acetonitrile (right). The contribution of solvent heating to $\Delta S_{iso}(q, t)$ for the dye solution was removed by using the SANOD method[2]. The contribution of solvent heating is absent for neat acetonitrile because the pump light is non-resonant with the electronic absorption of acetonitrile. **b**, (Left) The significant lSV of $\Delta S_{iso}(q, t)$ of the dye solution, $U_{iso}(q, dye)$. Here the lSV was multiplied by q to clearly visualize the fluctuation of the amplitudes at high scattering angles. (Right) Temporal amplitude profiles of the significant lSV. The temporal amplitude profile of the lSV for the dye solution was obtained multiplying the corresponding rSV by its singular value. The temporal amplitude profile of the lSV for neat acetonitrile was obtained by linear combination analysis of $\Delta S_{iso}(q, t)$ of neat acetonitrile with $U_{iso}(q, dye)$. Note that the lSV of the dye solution has significantly larger amplitude than that of neat acetonitrile.
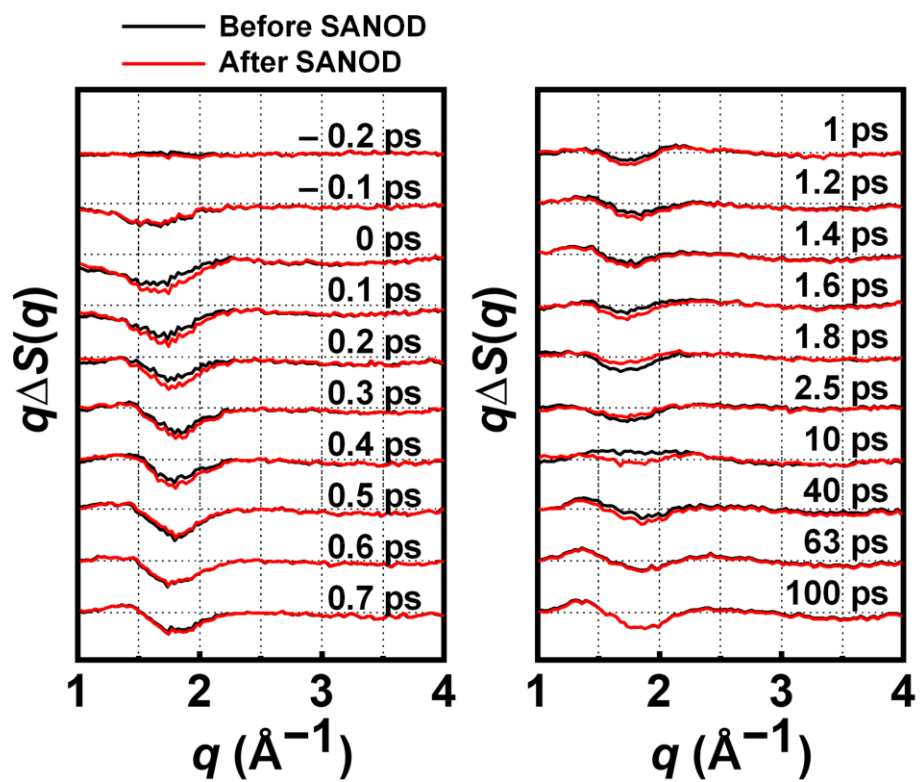
Figure S11. Comparison of the raw experimental X-ray difference scattering curves (black) and the data after artifact reduction using the SANOD method (red). The X-ray difference scattering curves of the dye solution in acetonitrile are shown.
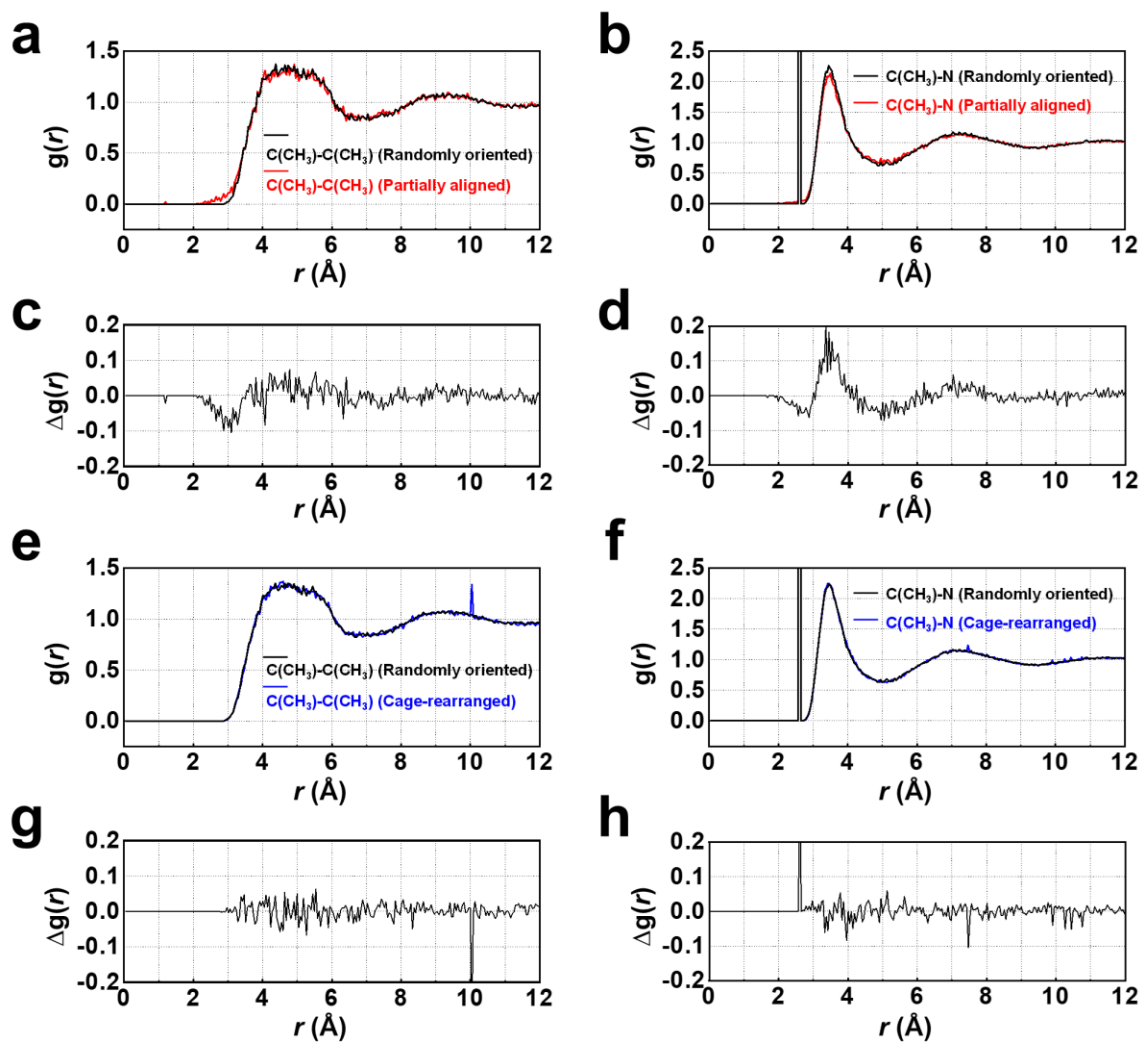
Figure S12. Theoretical RDFs calculated with ~5 % of aligned molecules for both the partially aligned and the cage-rearranged configurations. In Fig. 3b, for the emphasis of the perturbation of RDF, the RDFs were calculated with ~30 % of aligned molecules for the partially aligned configuration and ~5 % for the cage-rearranged configuration. In this figure, the comparison is made with the same fraction of the aligned molecules for the two configurations. **a–b**, The RDFs of (**a**) methyl carbon-methyl carbon and (**b**) methyl carbon-nitrogen pairs for the randomly oriented configuration (black) and the aligned configuration (red). **c–d**, The difference RDFs between the two configurations for (**c**) methyl carbon-methyl carbon and (**d**) methyl carbon-nitrogen pairs. It can be seen that, even for a small (~5 %) fraction of aligned molecules, the difference in RDFs of randomly oriented configuration and the partially aligned configuration is clearly visible. **e–f**, The RDFs of (**e**) methyl carbon-methyl carbon and (**f**) methyl carbon-nitrogen

pairs for the randomly oriented configuration (black) and the cage-rearranged configuration (blue). **g–h**, The difference RDFs between the two configurations for (**g**) methyl carbon-methyl carbon and (**h**) methyl carbon-nitrogen pairs. Details of the MD simulations are described in the Supporting Methods.
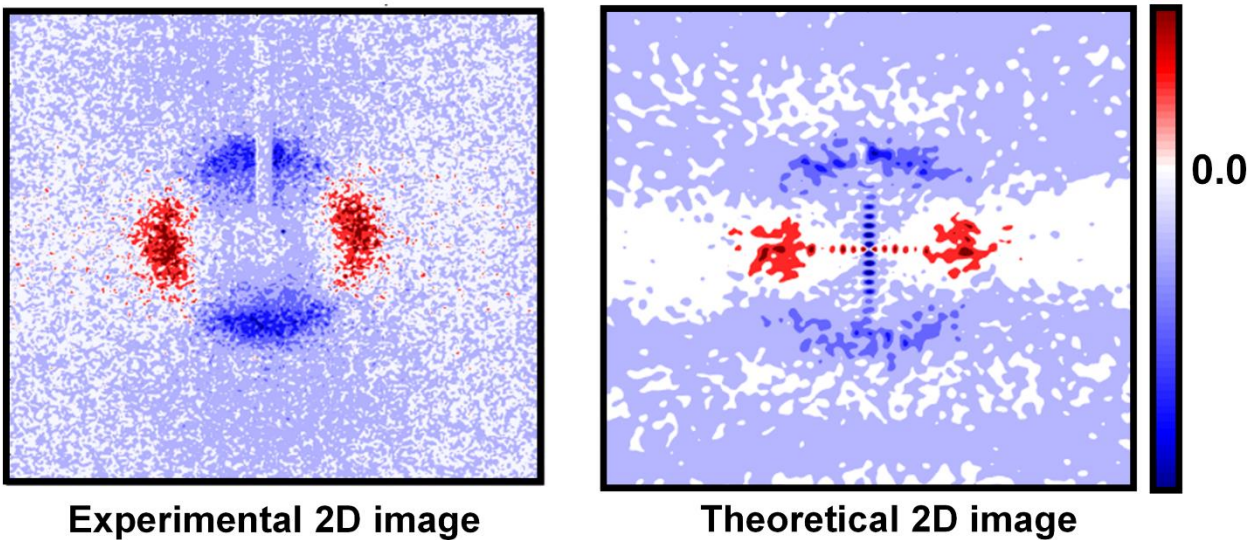
Experimental 2D image   **Theoretical 2D image**

Figure S13. Comparison of the experimental 2D difference scattering image (left) and the theoretical 2D difference scattering image (right). The experimental difference scattering image was measured at time zero for the dye solution in acetonitrile.